Available online at www.sciencedirect.com
ScienceDirect
Journal of Power Sources 172 (2007) 790–798
JOURNAL OF POWER SOURCES
www.elsevier.com/locate/jpowsour

A transient model of PEM fuel cells based on a spherical thin film-agglomerate approach

Shih-Ming Chang, Hsin-Sen Chu *

Department of Mechanical Engineering, National Chiao Tung University, HsinChu, Taiwan 300, ROC

Received 18 March 2007; received in revised form 7 May 2007; accepted 8 May 2007
Available online 18 May 2007

Abstract

The objective of this study is to investigate the transient behavior of a PEM fuel cell by using a one-dimensional, two-phase mathematical model. This model treats the catalyst layer as a spherical thin film-agglomerate. Effects of various transport parameter as well as other factors such as catalyst loading, gas diffusion layer thickness and liquid water permeability on the transient evolution of major model properties and cell performance are investigated in detail. Numerical results show that the evolution of ionic potential drop and oxygen consumption experience several steps before they reach steady state. The same situation can also be seen for the evolution of water saturation and current density. A detail inspection of these phenomena shows a close relation between these transport variables and cell performance. Parametric studies of other design factors' effects reveal there optimum values which lead to a greater current output during its evolution period.

Keywords: PEMFC; Transient analysis; Two-phase; Thin film-agglomerate model

1. Introduction

It is of great important to increase the performance of fuel cells (FCs) for modern consumer application such as portable and mobile devices. A number of studies have shown that the cathode is the most important fuel cell component, and its flooding problem is the major cause of performance deterioration in proton exchange membrane (PEM) fuel cells. One way to alleviate this phenomenon is by developing a better water management strategy. However, this requires a better understanding of electrochemical reactions and liquid water transport in the catalyst layers, which are the most complex components of the fuel cell.

Due to the extreme small geometry of the electrodes, it is difficult to directly measure the liquid water distribution in the gas diffusion layers and catalyst layers. Many researchers have developed mathematical models to investigate how liquid water transport affects the PEM fuel cell performance. Springer et al. [1] first developed an isothermal, one-dimensional, steady-state model for a complete polymer electrolyte fuel cell model. The model predicted an increase in membrane resistance with increased current density and demonstrated the great advantage of a thinner membrane in alleviating the resistance problem. Bernardi and Verbrugge [2,3] proposed a one-dimensional mathematical model of the solid-polymer-electrolyte (SPE) fuel cell for liquid water transport in porous electrodes assuming a constant liquid water volume fraction and no interactions between liquid and gas flows. A numbers of catalyst layer models had been developed, include the interface model [1–3], the thin film model [4], the agglomerate model [5–11], and the thin film-agglomerate model [12–14]. Using the agglomerate model, the researchers at National Research Council of Canada studied the optimum performance of PEM fuel cell for a number of optimization parameters: type of agglomerate, catalyst layer thickness, catalyst layer porosity, distribution of Nafion content, Pt loading, etc. [15–21]. Besides these models, the works of Wang and Wang [22,23] treated the catalyst layer as an individual zone with various conservation equations employed in the modeling of transient study and various time constants for the transient transport phenomena were proposed.

As for the investigation of two-phase flow, Wang et al. [24] pioneered the research on this issue through analytic and numer-

* Corresponding author. Tel.: +886 3 571 2121x55115; fax: +886 3 572 7930.
E-mail address: hschu@cc.nctu.edu.tw (H.-S. Chu).

0378-7753/$ – see front matter © 2007 Elsevier B.V. All rights reserved.
doi:10.1016/j.jpowsour.2007.05.017

Nomenclature

a	surface area per unit volume
b	Tafel slope
C_j	concentration of species j (mol cm^{-3})
D_j	diffusion coefficient of species j (cm^2 s^{-1})
F	Faraday constant
H	Henry constant (atm cm^3 mol^{-1})
i	current density (A cm^{-2})
k_c	condensation rate
k_T	oxygen reaction rate constant (s^{-1})
k_v	evaporation rate
K	permeability (cm^2)
M	molecular weight
N_j	molar flux of species j (mol cm^{-2} s^{-1})
P	pressure (atm)
r	radius (cm)
s	liquid water saturation level in porous medium
T	temperature (K)
V_s	cell potential (V)
y	mole fraction

Greek

δ	thickness (cm)
ε	porosity or volumetric fraction
ϕ	ionic potential (V)
φ	Thiele modulus
κ	conductivity (Ω^{-1} cm^{-1})
λ	water content
μ	viscosity (g cm^{-1} s^{-1})
ρ	density (g cm^{-1})
τ	tortuosity
ξ	effectiveness factor

Subscripts and superscripts

agg	agglomerate
CL	catalyst layer
eff	effective
g	gas phase
GDL	gas diffusion layer
MEM	membrane
N	Nafion phase
O_2	oxygen
p	proton
Pt	platinum
sat	saturation
v	vapor water
w	liquid water

ical methods. A threshold current density was proposed to distinguish the scenarios between single- and two-phase regimes of water distribution and transport. In the subsequent works of their group, sophisticated models [25–28] were developed to simulate the flooding and liquid water distribution in PEM fuel cells. The mature multiphase mixture (M^2) formulation with single set of conservation equations was employed to mimic the two-phase transport process. The results showed that it is important to consider the gas-phase pressure field in the GDL as a new mechanism of reactant transport. Another analytic model performed by Pasaogullari et al. [29], focusing on the liquid water transport in hydrophobic electrode, indicated that capillary transport dominates the water remove from flooded GDL. The model of Natarajan and Van Nguyen [30,31], which considered the evaporation or condensation of liquid water, also demonstrated the importance of its transport on cell performance. Moreover, comprehensive review summarizing the current statues of the fuel cell modeling as well as point the development direction of this emerging field is presented by Wang [32].

With the consideration that the catalyst layer is the most important component in the electrochemical reaction of a fuel cell, also the experimental results of TEM images by Siegel et al. [7] clearly showed that carbon-supported, spherical Pt pellets exist in the catalyst layers. To mimic the actual morphology of the catalyst layers, a spherical thin film-agglomerate expression along with a one-dimensional, two-phase model is developed in this paper to investigate the transient evolutions of various model properties as well as cell performance. The boundary conditions at the CL/membrane interface also take into account the effects of water content on certain design parameters such as GDL permeability, CL permeability, catalyst loading, and GDL thickness.

2. Mathematical modeling

This study presents a transient analysis of a PEM fuel cell cathode. The model domain consists of a gas diffusion layer (GDL), a catalyst layer (CL), and a membrane, arranged as shown in Fig. 1. Our previously published cylindrical thin film-agglomerate model [13] is extended to a spherical model in this work. The electrochemical kinetics and transport of oxygen, vapor water, and liquid water are also analyzed in the GDL, CL, and proton exchange membrane (PEM). When the PEM fuel cell is turned on, air diffuses through the GDL from the channel to the catalyst layer. Meanwhile, oxygen dissolves into the Nafion film and eventually reaches the pellet surface, where liquid water is generated. The following assumptions are made:

(1) The gas-phase obeys the ideal gas law.
(2) Electronic resistance is negligible in the GDL and CL.
(3) CL and GDL are assumed hydrophilic.
(4) The catalyst pellets are spherical, consist of carbon-supported platinum and Nafion, and are covered by a Nafion film.
(5) All the catalyst pellets in the CL have the same radius and Nafion film thickness.
(6) The catalyst pellets are homogeneous, and oxygen diffuses into them via the Nafion film.
(7) The oxygen reduction reaction generates only liquid-phase water.
(8) The ionic potential between the anode catalyst layer and the membrane is approximately zero, because the hydrogen oxidation reaction is fast.

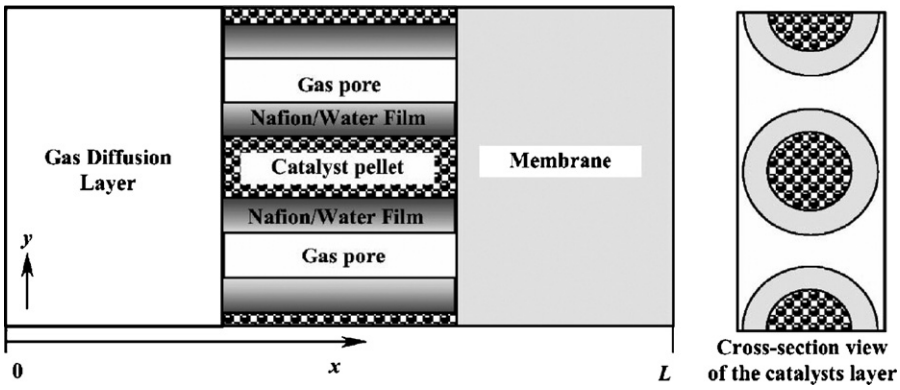

Fig. 1. Schematic of the model [12].

Our previous paper [13] provides details on the derivation of the model. The conservation equations applied are listed in Table 1, for the following five variables:

(1) The concentration of oxygen in the gas-phase, $[C_{O_2}^{g}]$.
(2) The concentration of water vapor in the gas-phase, $[C_{v}^{g}]$.
(3) The liquid water saturation level, $[s]$ (the ratio between liquid water volume and void volume in the porous medium).
(4) The concentration of liquid water in the Nafion phase, $[C_{w}^{N}]$.
(5) The ionic potential, $[\phi]$ (in the Nafion phase).

Experimental studies [5,7] have shown that the carbon-supported Pt catalysts in the CL are approximately spherical. As mentioned above, this investigation treats them as perfect spheres. The derivation of spherical thin film-agglomerate model described here is based on the cylindrical models of Lin et al. [12] and Chang and Chu [13]. The principal difference between the cylindrical model and the spherical model is the outer surface area per unit volume of the agglomerate. The surface area per unit volume of the agglomerate is defined as,

$$a_r = \frac{\text{Agglomerate's surface area}}{\text{Geometric volume}} \tag{1}$$

For spherical thin film-agglomerate model, a_r is:

$$\begin{aligned} a_r &= \frac{4\pi(r_p+\delta_N)^2}{(4/3)\pi(r_p+\delta_N)^3/(1-\varepsilon_0^{CL})} \\ &= \frac{3}{(r_p+\delta_N)}(1-\varepsilon_0^{CL}) \end{aligned} \tag{2}$$

The initial values of all variables are zero, except for the liquid water concentration in the Nafion phase which is assumed to be in equilibrium with the water vapor activity in the gas-phase. All boundary conditions are listed in Table 2. The CL/membrane interface boundary condition for the concentration of liquid water in the Nafion phase (Eq. (3)) is taken from the model of Lin and Nguyen [14], where the water content below 14 mol H_2O (mol SO_3^-)$^{-1}$ was determined by water vapor activity. When the gas stream is saturated, however, and liquid water exists in the pores of the CL (between 14 and 16.8 mol H_2O (mol SO_3^-)$^{-1}$), the water content varies linearly with the liquid water saturation level [1]. Since liquid water is generated when a fuel cell starts up, any liquid water in the CL/MEM interface pores can dissolve into the Nafion phase. This leads to the boundary condition:

$$C_w^{N,eq} = (0.043 + 17.81\alpha - 39.8\alpha^2 + 36.0\alpha^3)C_f + 2.8C_f s, \tag{3}$$

where α is the water activity in the gas-phase in the CL cathode and C_f is the concentration of fixed charged sites in the membrane.

All the correlations used in this model are listed in Table 3.

The governing equations and boundary conditions are discretized by the finite difference method. The convergence criteria for a steady state are:

$$\left|\frac{V_i^{new} - V_i^{old}}{V_i^{old}}\right| \le 1 \times 10^{-4} \tag{4}$$

where V_i is an arbitrary variable.

3. Results and discussion

Water management plays an important role on the performance of PEM fuel cells. Understanding their starting process and performance evolution are also crucial in the actual operating applications. Simulation results for this issue by employing the PEM fuel cell cathode model is presented in the following sections. Investigations on how the structural parameters of the cell such as GDL permeability, CL permeability, catalyst loading, and GDL thickness affect its performance are also demonstrated.

To validate the numerical model, the comparison of calculation results and Navessin et al.'s experimental results are carried out. The comparison results are shown in Fig. 2. The experimental operating conditions and parameters of Navessin et al. are listed in Table 4, and those of the model are listed in Table 5. The *I–V* polarization curve represents the fuel cell's steady state at an operating temperature of 25 °C. The PEM fuel cell operates under uniform conditions from the time it is turned on until a steady state is achieved. It is found that current model results agree well with the experimental data.

Table 1
Governing equations

Variables	GDL	CL	MEM
$C^{g}_{O_2}$	$\frac{\partial}{\partial t}((1-s)\varepsilon_0^{GDL}C^{g}_{O_2}) = D_{O_2}\varepsilon_0^{GDL^{\tau}}\left[(1-s)\right]^{\tau}\nabla^2 C^{g}_{O_2} + \nabla\cdot[(1-s)]^{\tau}\nabla\cdot C^{g}_{O_2}\right]$	$\frac{\partial}{\partial t}((1-s)\varepsilon_0^{GL}C^{g}_{O_2}) = -R_{O_2} + D_{O_2}\varepsilon_0^{GL^{\tau}}\left[(1-s)\right]^{\tau}\nabla^2 C^{g}_{O_2} + \nabla\cdot[(1-s)]^{\tau}\nabla\cdot C^{g}_{O_2}\right]$	–
C^{g}_{v}	$\frac{\partial}{\partial t}((1-s)\varepsilon_0^{GDL}C^{g}_{v}) = -R_w + D_v\varepsilon_0^{GDL^{\tau}}\left[(1-s)\right]^{\tau}\nabla^2 C^{g}_{v} + \nabla\cdot[(1-s)]^{\tau}\nabla\cdot C^{g}_{v}\right]$	$\frac{\partial}{\partial t}((1-s)\varepsilon_0^{GL}C^{g}_{v}) = -R_w + D_v\varepsilon_0^{GL^{\tau}}\left[(1-s)\right]^{\tau}\nabla^2 C^{g}_{v} + \nabla\cdot[(1-s)]^{\tau}\nabla\cdot C^{g}_{v}\right]$	–
s	$\frac{\varepsilon_0^{GDL}\rho_w}{M_w}\frac{\partial s}{\partial t} = R_w + \frac{\rho_w K_{w,0}}{M_w\mu_w}\left(-\frac{dP_c}{ds}\right)(s\nabla^2 s + (\nabla\cdot s)^2)$	$\frac{\varepsilon_0^{GL}\rho_w}{M_w}\frac{\partial s}{\partial t} = (4n_d^{CL}+2)R_{O_2} + R_w + \frac{\rho_w K_{w,0}}{M_w\mu_w}\left(-\frac{dP_c}{ds}\right)(s\nabla^2 s + (\nabla\cdot s)^2)$	–
C^{N}_{w}	–	$\varepsilon_m^{CL}\frac{\partial C^{N}_{w}}{\partial t} = D^{N}_{w}\nabla^2 C^{N}_{w}$	$\varepsilon_m\frac{\partial C^{N}_{w}}{\partial t} = D^{N}_{w}\nabla^2 C^{N}_{w} + \frac{n_d i_N}{F}\nabla^2 V_+$
ϕ	–	$K_{N,eff}\nabla^2\phi - 4FR_{O_2} = 0$	$\nabla^2\phi = 0$

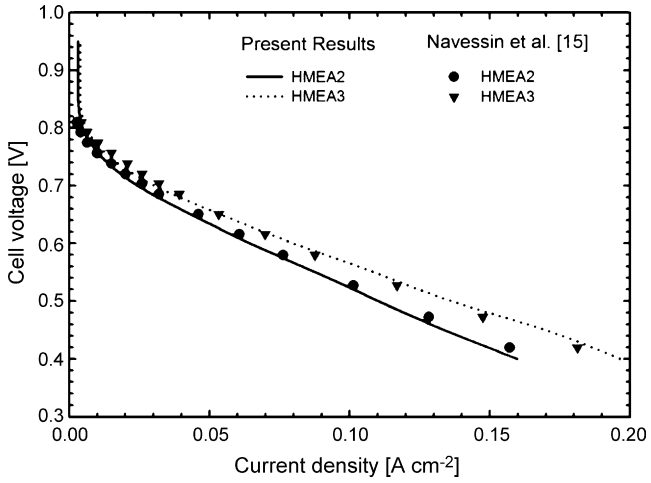

Fig. 2. A comparison of the model to experimental data.

Fig. 3 displays the evolution of the total ionic potential drop (IPD) in the catalyst layer, for three different cell potentials V_s.

$$\mathrm{IPD} = \sum_{x=\mathrm{GDL}}^{x=\mathrm{CL}} (\phi_p|_{x=\mathrm{CL}} - \phi_p(x)). \tag{5}$$

This plot can be divided into five sections: (1) a rapid rise, which lasts from startup to 0.01 s; (2) from 0.01 to 0.1 s, the potential plateaus (remains approximately constant); (3) at 0.1 s the potential rises rapidly again to its maximum value; (4) the potential drops again; (5) a second plateau is reached representing the steady state.

The total dimensionless oxygen consumption (TOC) in the catalyst layer also evolves over time, as shown in Fig. 4. This quantity is defined as:

$$\mathrm{TOC} = \sum_{x=\mathrm{GDL}}^{x=\mathrm{CL}} \frac{C^{g}_{O_2}|_{x=\mathrm{GDL}} - C^{g}_{O_2}(x)}{C^{g,\mathrm{inlet}}_{O_2}}. \tag{6}$$

The plot can be divided into six sections: (1) a rapid rise from startup to 5×10^{-3} s; (2) the first plateau, which lasts from

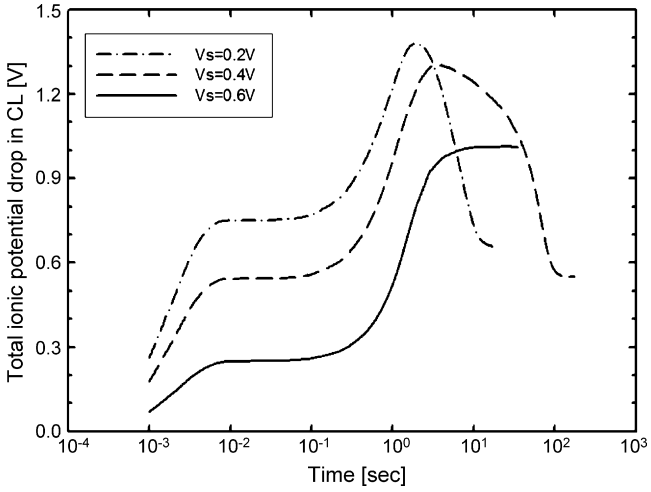

Fig. 3. Evolution of the total ionic potential drop in the catalyst layer under various cell voltages.

Table 2
Boundary conditions

Variables	$X=0$	GDL/CL	CL/MEM	$X=L$
$C^{g}_{O_2}$	$C^{g}_{O_2} = C^{air}_{O_2}$	$N^{g}_{O_2}\|_{GDL} = N^{air}_{O_2}\|_{GDL}$	$N^{g}_{O_2}\|_{CL} = 0$	–
C^{g}_{v}	$C^{g}_{v} = C^{air}_{v}$	$N^{g}_{v}\|_{GDL} = N^{air}_{v}\|_{GDL}$	$N^{g}_{v}\|_{CL} = 0$	–
s	$s=0$	$N_w\|_{GDL} = N_w\|_{GDL}$	$N_w\|_{CL} = 0$	–
C^{N}_{w}	–	$N^{N}_{w}\|_{GDL} = 0$	$C^{N,eq}_{w} = (0.043 + 17.81\alpha - 39.8\alpha^2 + 36.0\alpha^3)C_f + 2.8C_f s$	$C^{N}_{w}\|_{MEM} = C^{N,eq}_{w(anode)}$
ϕ	–	$i_p\|_{GDL} = 0$	$i_p\|_{CL} = i_p\|_{CL}$	$\phi=0$

Table 3
Correlations used in this study

Diffusivity of oxygen in Nafion membrane [3] ($cm^2\ s^{-1}$)	$D^{N}_{O_2} = 0.0031 \exp\left(-\frac{2768}{T}\right)$
Diffusivity of oxygen in liquid water ($cm^2\ s^{-1}$)	$D^{W}_{O_2} = 2.14 \times 10^{-5}\left(\frac{\mu_{T_r}}{\mu_T}\right)^{1.026}\left(\frac{T}{T_r}\right)$
Diffusivity of oxygen in gas stream [33] ($cm^2\ s^{-1}$)	$D^{g}_{O_2} = 0.1775\left(\frac{T}{273.15}\right)^{1.823}$
Diffusivity of vapor water in gas stream [33] ($cm^2\ s^{-1}$)	$D^{g}_{v} = 0.256\left(\frac{T}{307.15_r}\right)^{2.334}$
Henry's constant for oxygen between Nafion and air [3] ($cm^3\ mol^{-1}$)	$H^{N}_{O_2} = 1.33 \times 10^{6}\exp\left(\frac{-498}{T}\right)$
Henry's constant for oxygen between liquid water and air [34] ($cm^3\ mol^{-1}$)	$H^{N}_{O_2} = 1.33 \times 10^{6}\exp\left(\frac{-498}{T}\right)$
Water content	$\lambda = \frac{C^{N}_{w}}{C_f}$
Net electro-osmotic drag coefficient [1]	$n_d = \frac{2.5}{22\lambda}$
Conductivity of Nafion membrane [1] ($(\Omega\,cm)^{-1}$)	$\kappa_N = \exp\left[1268\left(\frac{1}{303} - \frac{1}{T}\right)\right](0.005139\lambda - 0.00326)$
Diffusivity of liquid water in Nafion membrane [1] ($cm^2\ s^{-1}$)	$C^{N}_{w(2>\lambda\geq 3)} = 10^{-6}\exp\left[2416\left(\frac{1}{303} - \frac{1}{T}\right)\right](-3.1 + 2.0\lambda)$ $C^{N}_{w(3>\lambda\geq 4)} = 10^{-6}\exp\left[2416\left(\frac{1}{303} - \frac{1}{T}\right)\right](6.89 - 1.33\lambda)$ $C^{N}_{w(\lambda>4)} = 10^{-6}\exp\left[2416\left(\frac{1}{303} - \frac{1}{T}\right)\right](2.563 - 0.33\lambda + 0.0246\lambda^2 - 0.000671\lambda^3)$

5×10^{-3} to 5×10^{-2} s (consumption increases slightly during this phase); (3) another rise from 5×10^{-2} to 0.5 s; (4) a second plateau from 0.5 to 2 s (where the consumption decreases slightly); (5) a rapid rise to the peak value from 2 s onward; finally (6) a steady-state plateau. Oxygen consumption increases less than 15% in the first plateau, and decreases by only 2% in the second plateau. As the IPD increases, the fuel cell must overcome higher and higher activation energies to maintain a higher rate of electrochemical reaction. After the fuel cell overcomes

Table 4
Parameters used by Navessin et al. [15]

Gas diffusion layer properties	
Porosity	0.6
Thickness (cm)	0.035
Catalyst layer properties	
Porosity	0.55
Thickness (cm)	0.005
Catalyst loading (mpt) (mg)	0.78
Area per unit volume[a] (m^{-1})	727,664
Volumetric fraction of Naion in catalyst pellet (ε^{P}_{N})	0.2
Raduis of catalyst pellet, (R_{agg}) (cm)	2.5×10^{-5}
Exchange current density[a] ($mA\ cm^{-2}$)	1.27, 1.66
Reference concentration of O_2, ($C_{O_2,ref}$)[a] ($\mu mol\ cm^{-3}$)	2.34, 2.25
Membrane properties	
Porosity	0.35
Thickness[a] (cm)	0.0062, 0.0061
Operation conditions	
Temperature (°C)	25.0
Pressure (atm)	1.0

[a] List value for HMEA-2 and HMEA-3, respectively.

Table 5
Parameters used in this simulation (base case)

Gas diffusion layer properties	
Porosity	0.3
Thickness (cm)	0.025
Permeability (cm^2)	10^{-9}
$\left(-\frac{dp_c}{ds}\right)$ ($Dyne\ cm^{-2}$)	284.2
Catalyst layer properties	
Porosity	0.06
Thickness (cm)	0.0016
Permeability (cm^2)	3×10^{-11}
$\left(-\frac{dp_c}{ds}\right)$ ($Dyne\ cm^{-2}$)	568.4
Catalyst loading (m_{Pt}) (mg)	0.4
Specific surface area of Pt (a_{Pt}) (cm^2(mg Pt)$^{-1}$)	1000
Volumetric fraction of Nafion in catalyst pellet (ε^{P}_{N})	0.393
Radius of catalyst pellet (R_{agg}) (cm)	10^{-5}
Thickness of Nafion (cm)	10^{-6}
Exchange current density ($i_{0,ref}$ 0 °C) ($A\ cm^{-2}$)	10^{-6}
Membrane properties	
Thickness (cm)	0.005
Porosity	0.35
Fixed charge site concentration ($mol\ cm^{-3}$)	1.2×10^{-3}
Operation conditions	
Temperature (°C)	60.0
Pressure (atm)	1.0
Mole fraction of O_2 in inlet	0.206
Humidity in inlet (%)	10
Humidity at anode (%)	100

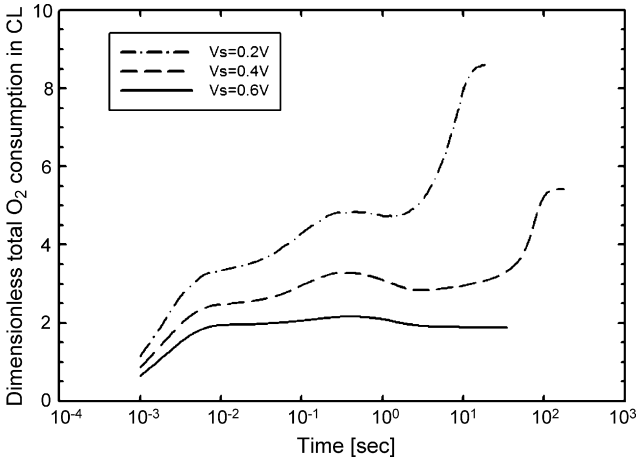

Fig. 4. Evolution of the total dimensionless oxygen consumption in the catalyst layer under various cell voltages.

the maximum activation energy, the IPD decreases. As shown in Fig. 4, when $V_s = 0.2$ V and 0.4 V, after 2 s, the TOC increases rapidly. Thus, after a fuel cell overcomes the maximum activation energy, it retains a high electrochemical reaction rate with a lower IPD.

Fig. 5 shows the evolution of the liquid water saturation level, measured at various cell voltages. The liquid water saturation level plot can be divided into four sections. From startup to 10^{-2} s, liquid water accumulates in the catalyst layer. Between 10^{-2} and 0.5 s, liquid water begins diffusing into the gas diffusion layer. During the next phase, from 0.5 to 2 s, the liquid water saturation level in the CL decreases as more and more liquid water occupies pores in the GDL. In the final phase, the liquid water saturation level increase in both CL and GDL until a steady state is reached. Although the liquid water saturation level decreases in the CL between 0.5 and 2 s, note that it will increase again once the electrochemical reaction rate generates enough liquid water to fill the Nafion phase. When $V_s = 0.6$ V, for example, the electrochemical reaction rate is moderate and less liquid water is generated. In this case, at the time after 2 s, the liquid water saturation level decreases (Fig. 5c). In contrast, the liquid water saturation level increases after 2 s for $V_s = 0.2$ and 0.4 V (Fig. 5a and b).

The fuel cell cannot be turned on if the Nafion phase is completely dry, so it is assumed that the concentration of liquid water in the Nafion phase is equal to the concentration of fixed charge sites at the anode. Fig. 6 shows the evolution of the CL water content over time at three different cell voltages. These plots can be divided into three sections: from startup to 3 s, the water content decreases; from 3 to 13 s, the water content increases; and in the final phase, the water content is constant. Initially there is less liquid water amount in the gas pores than in the Nafion phase, so at first liquid water flows from the Nafion phase to the gas pores. When more liquid water begins to be generated, it dissolves into the Nafion phase again and we see increasing water content in both the CL and the membrane.

The current density evolution for various cell voltages is shown in Fig. 7. These plots can be divided into five sections. From startup to 5×10^{-3} s, the current density rises rapidly.

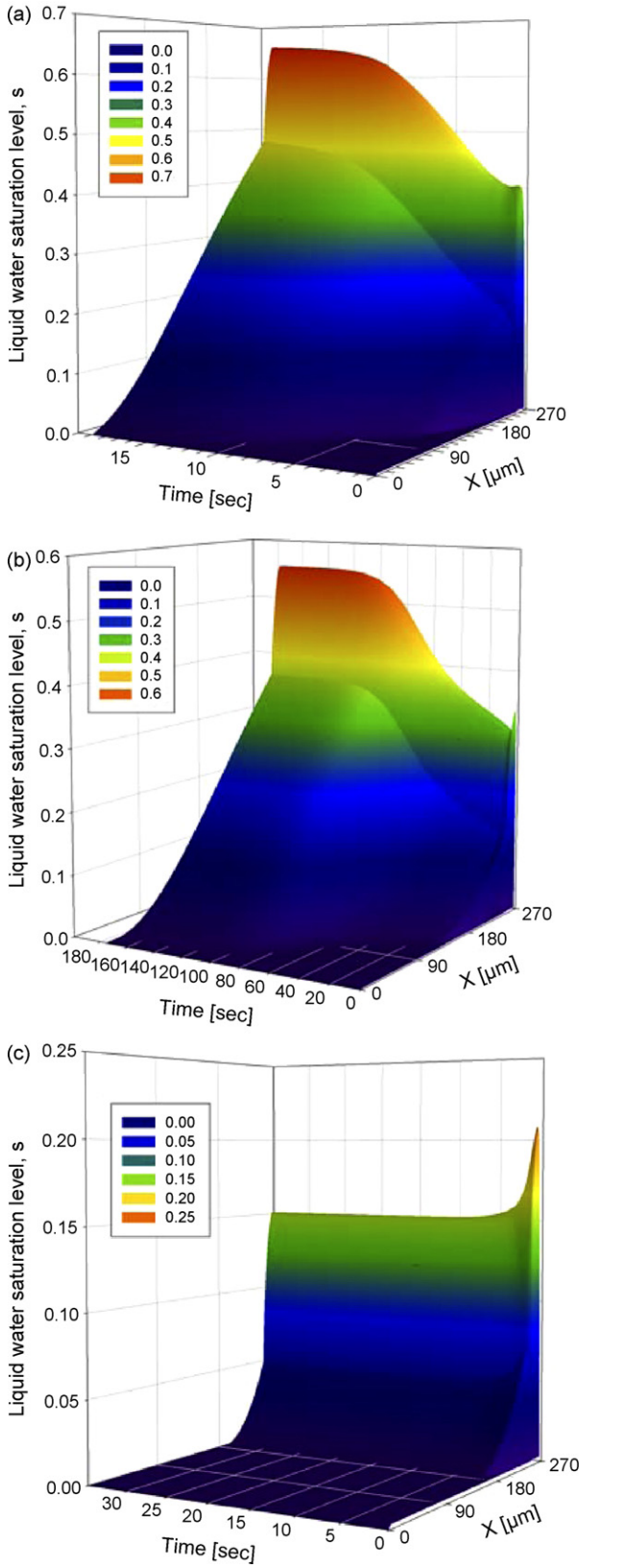

Fig. 5. Evolution of the liquid water saturation level under various cell voltages, (a) $V_s = 0.2$ V, (b) $V_s = 0.4$ V and (c) $V_s = 0.6$ V.

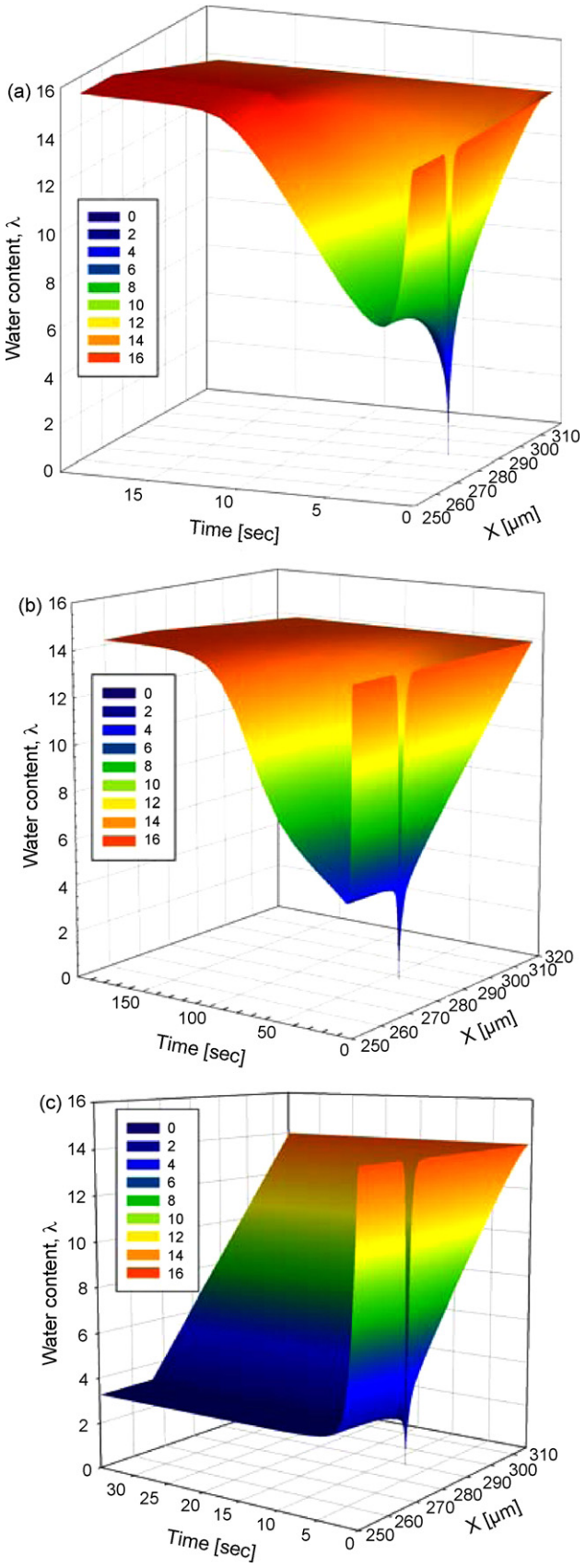

Fig. 6. Evolution of the water content under various cell voltages, (a) $V_s = 0.2$ V, (b) $V_s = 0.4$ V and (c) $V_s = 0.6$ V.

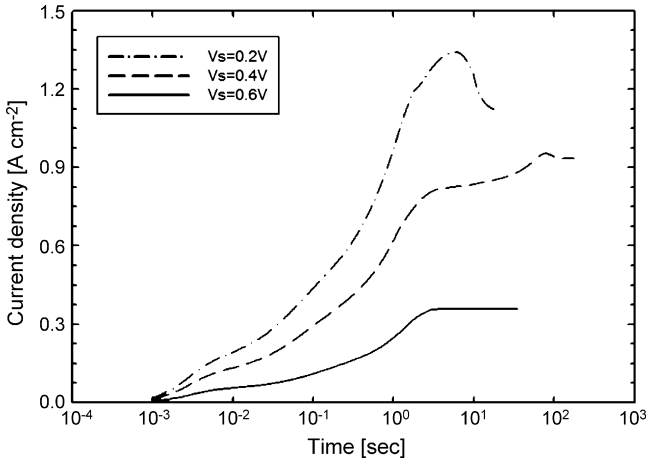

Fig. 7. Evolution of the current density under various cell voltages.

From 5×10^{-3} to 2×10^{-2} s, the current density plateaus. The current density begins to rise rapidly again at 2×10^{-2} s, eventually reaching its maximum value, then drops briefly. Finally, it reaches a steady-state plateau. As seen in Fig. 5, liquid water hinders oxygen transport as it diffuses from the CL to the GDL. The electrical conductivity is also reduced during this period, due to decreased water content, and the current density levels off as a result. Note that the total oxygen consumption increases rapidly after 0.05 s (Fig. 4), and that the ionic potential drop increases rapidly after 0.1 s (Fig. 3). Thus, the current density increases rapidly after 0.1 s. Oxygen transport resistance increases after 0.1 s, however, because at this point the liquid water saturation level is increasing in both GDL and CL (Fig. 5). Thus, the current density levels off after 1 s.

The current density drops off after reaching its maximum value for the following reason. The higher the current density, the more liquid water is generated and the more gas pores are occupied by liquid water. When this happens, however, the catalyst pellets also have less oxygen on their exposed surface. This tends to reduce the electrochemical reaction rate and causes a drop in the current density. At lower cell voltages the electrochemical reaction rate is higher, so more liquid water is generated and we see a more extreme drop in the current density. For instance, when $V_s = 0.2$ V the drop is more than 30%.

Fig. 8 shows the effect of modifying GDL permeability for $V_s = 0.4$ V. Cases 1 through 4 used permeabilities of 9×10^{-10}, 1×10^{-9}, 1×10^{-8}, and 1×10^{-7} cm^2, respectively. The higher the permeability, the more liquid water will be drained; this lowers the amount of liquid waver available and reduces the current density. If the GDL permeability is too low, however, liquid water cannot drain effectively. This will reduce the available oxygen on the catalyst surface, decreasing cell performance and limiting mass transport.

Fig. 9 examines the effect of CL permeability when $V_s = 0.4$ V; cases 1 through 4 use values of 8×10^{-12}, 3×10^{-11}, 3×10^{-10}, and 3×10^{-9} cm^2, respectively. Cases 3 and 4 have the highest permeabilities and effective water drainage. But when liquid water drains from the fuel cell quickly, it also reduces the water content of the Nafion phase. Thus, a lower

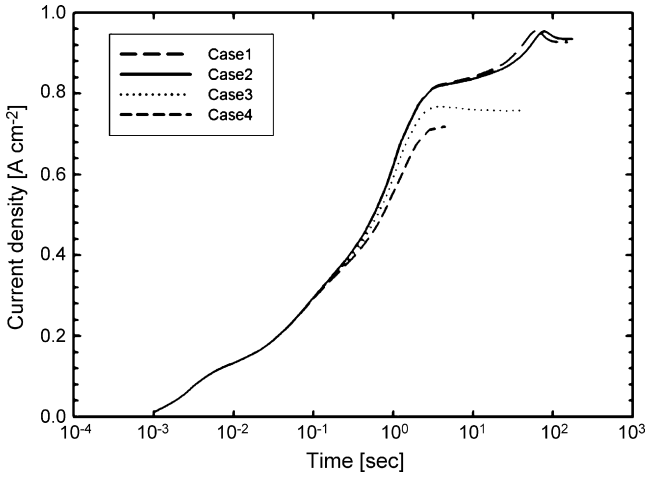

Fig. 8. The effect of GDL permeability on the current density ($V_s = 0.4$ V).

CL permeability means that there will be more liquid water in the Nafion phase. The maximum current densities achieved in cases 1 and 2 are similar, but the steady-state current density in case 2 is higher. This is because in case 1, liquid water is occupying more of the gas pores and effectively covering the catalyst pellet surface, causing a series concentration overpotential.

The current density evolution for $V_s = 0.4$ V is shown in Fig. 10, under catalyst loadings of 0.2, 0.3, 0.4, and 0.5 mg for cases 1 through 4, respectively. A higher catalyst loading means a more rapid electrochemical reaction. The current densities in cases 1 and 2 are obviously lower than those in cases 3 and 4, because the catalyst loading is too low in the former to drive the reaction. The maximum current density in case 4 drops rapidly, on the other hand, because of fuel cell flooding. Oxygen cannot reach the surface of the catalyst pellets when there is too much liquid water. This suggests that excessive catalyst loading does not improve cell performance.

Finally, Fig. 11 demonstrates the evolution of current density for $V_s = 0.4$ V under various thicknesses of the gas diffusion layer. Through case 1 to 6, the thicknesses are 220, 235, 240, 245, 250, and 265 μm, respectively. The current density increases to a constant (steady state) value after 2 s for GDL layers less than or equal to 240 μm thick. For the remaining cases, the current density rises again after 2 s, reaches its maximum, then decreases in value and reaches a steady state. A thicker gas diffusion layer means a higher maximum current density, but this value may overshoot the sustainable current. Thicker GDL also imposes a greater resistance to liquid water transport, which promotes flooding of the fuel cell. Liquid water drains more quickly with a thinner gas diffusion layer, but the fuel cell cannot be too dry or its performance will deteriorate.

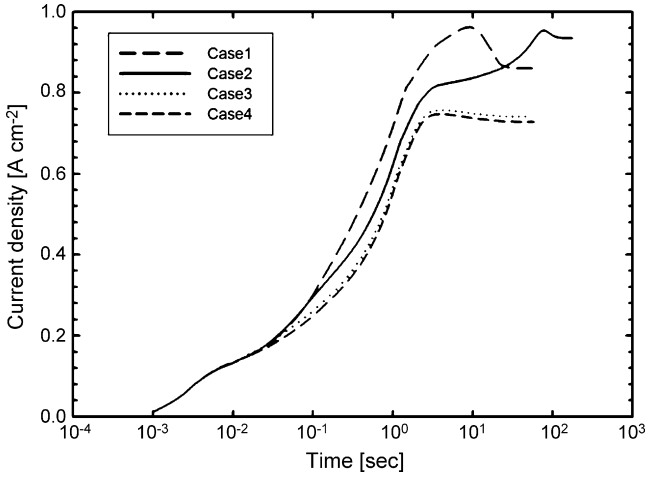

Fig. 9. The effect of CL permeability on the current density ($V_s = 0.4$ V).

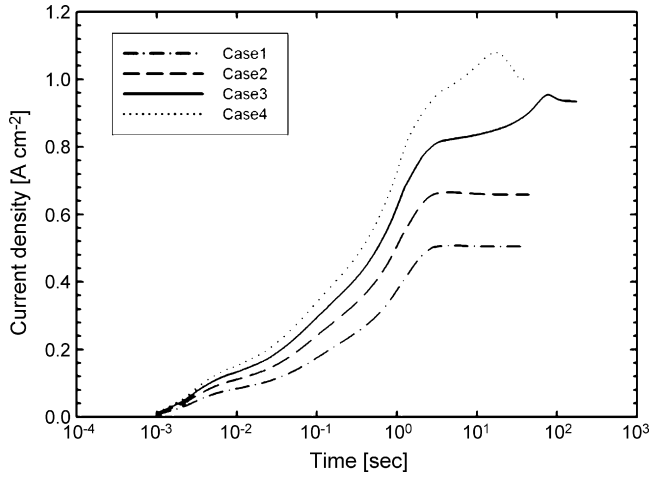

Fig. 10. The effect of catalyst loading on the current density ($V_s = 0.4$ V).

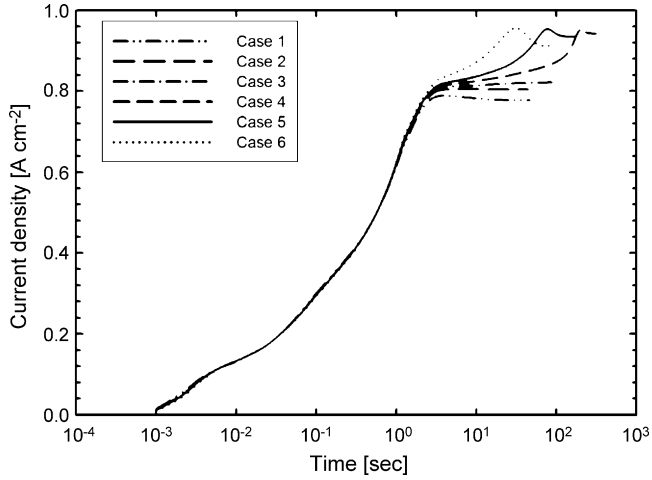

Fig. 11. The effect of GDL thickness on the current density ($V_s = 0.4$ V).

4. Conclusion

A transient, one-dimensional, two-phase model of a PEM fuel cell cathode is presented in this study with the catalyst layer treated as a spherical thin film-agglomerate. This model is used to investigate the transient transport of gaseous species, protons, and liquid water. The effects of GDL permeability, CL permeability, catalyst loading, and GDL thickness on cell performance are also investigated.

Our model results agree well with the experimental data. The observed IPD and TOC variations show that after the fuel cell

overcomes its maximum activation energy, a high electrochemical reaction rate with low IPD is maintained. Electrochemical reactions affect the amount of liquid water in the cell; when less water is generated, the cell reaction rate is reduced. Nevertheless, the higher liquid water content and saturation level tend to lead to the flooding catastrophe.

Parametric sensitivity analysis also shows that at higher permeability, more liquid water is able to drain from the cell. Cell performance will decrease if there is too little liquid water, but may also be influenced if the water cannot drain effectively. Among the values adopted in this paper, the optimum GDL permeability is $K_{w,0}^{GDL} = 1 \times 10^{-9}\,cm^2$ and the optimum CL permeability is $K_{w,0}^{GL} = 3 \times 10^{-11}\,cm^2$.

Moreover, a cell with higher catalyst loading leads to more rapid electrochemical reactions, but this may also result in too much liquid water generation. This ultimately impedes oxygen transport, so excessive catalyst loading does not improve cell performance. Among the values considered in this study, the optimum loading is $m_{Pt} = 0.4\,mg$.

Finally, GDL thickness was found to play an important role in liquid water transport. A thinner layer offers less resistance to liquid water diffusion and drainage. Water content and cell performance therefore tend to remain constant. When the gas diffusion layer is thick, liquid water cannot drain effectively and the catalyst pellets will have less surface oxygen. According to these results, the optimum thickness is $\delta_{GDL} = 245\,\mu m$.

Fuel cell performance and durability are also strongly influenced by impurities in the hydrogen gas used. A particular level of carbon monoxide yields a stable performance loss. Therefore, another research topic which is currently undergoing in our group is the investigation of the CO poisoning effect with the thin film-agglomerate model.

References

[1] T.E. Springer, T.A. Zawodzinski, S. Gottesfeld, J. Electrochem. Soc. 138 (1991) 2334–2342.
[2] D.M. Bernardi, M.W. Verbrugge, J. Electrochem. Soc. 139 (1992) 2477–2491.
[3] D.M. Bernardi, M.W. Verbrugge, AIChE J. 37 (1991) 1151–1163.
[4] Y.W. Rho, S. Srinivasan, Y.T. Kho, J. Electrochem. Soc. 141 (1994) 2089–2096.
[5] K. Broka, P. Ekdunge, J. Appl. Electrochem. 27 (1997) 281–289.
[6] F. Jaouen, G. Lindbergh, G. Sundholm, J. Electrochem. Soc. 149 (2002) A437–A447.
[7] N.P. Siegel, M.W. Ellis, D.J. Nelson, M.R. von Spakovsky, J. Power Sources 115 (2003) 81–89.
[8] N.P. Siegel, M.W. Ellis, D.J. Nelson, M.R. von Spakovsky, J. Power Sources 128 (2004) 173–184.
[9] W. Sun, B.A. Peppley, K. Karan, J. Power Sources 144 (2005) 42–53.
[10] W. Sun, B.A. Peppley, K. Karan, Electrochim. Acta 50 (2005) 3359–3374.
[11] K.M. Yin, J. Electrochem. Soc. 152 (2005) A583–a593.
[12] G.Y. Lin, W.S. He, T. Van Nguyen, J. Electrochem. Soc. 151 (2004) A1999–A2006.
[13] S.-M. Chang, H.-S. Chu, J. Power Sources 161 (2006) 1161–1168.
[14] G. Lin, T. Van Nguyen, J. Electrochem. Soc. 153 (2006) A372–A382.
[15] T. Navessin, S. Holdcroft, Q.P. Wang, D.T. Song, Z.S. Liu, M. Eikerling, J. Horsfall, K.V. Lovell, J. Electroanal. Chem. 567 (2004) 111–122.
[16] D.T. Song, Q.P. Wang, Z.S. Liu, M. Eikerling, Z. Xie, T. Navessin, S. Holdcroft, Electrochim. Acta 50 (2005) 3347–3358.
[17] D.T. Song, Q.P. Wang, Z.S. Liu, T. Navessin, M. Eioerling, S. Holdcroft, J. Power Sources 126 (2004) 104–111.
[18] D.T. Song, Q.P. Wang, Z.S. Liu, T. Navessin, S. Holdcroft, Electrochim. Acta 50 (2004) 731–737.
[19] Q.P. Wang, M. Eikerling, D.T. Song, Z.S. Liu, J. Electroanal. Chem. 573 (2004) 61–69.
[20] Q.P. Wang, M. Eikerling, D.T. Song, Z.S. Liu, T. Navessin, Z. Xie, S. Holdcroft, J. Electrochem. Soc. 151 (2004) A950–a957.
[21] Q.P. Wang, D.T. Song, T. Navessin, S. Holdcroft, Z.S. Liu, Electrochim. Acta 50 (2004) 725–730.
[22] Y. Wang, C.Y. Wang, Electrochim. Acta 50 (2005) 1307–1315.
[23] Y. Wang, C.-Y. Wang, Electrochim. Acta 51 (2006) 3924–3933.
[24] Z.H. Wang, C.Y. Wang, K.S. Chen, J. Power Sources 94 (2001) 40–50.
[25] U. Pasaogullari, C.Y. Wang, Electrochim. Acta 49 (2004) 4359–4369.
[26] U. Pasaogullari, C.Y. Wang, J. Electrochem. Soc. 152 (2005) A380–A390.
[27] H. Meng, C.-Y. Wang, J. Electrochem. Soc. 152 (2005) A1733–A1741.
[28] Y. Wang, C.-Y. Wang, J. Electrochem. Soc. 153 (2006) A1193–A1200.
[29] U. Pasaogullari, C.Y. Wang, K.S. Chen, J. Electrochem. Soc. 152 (2005) A1574–A1582.
[30] D. Natarajan, T. Van Nguyen, J. Electrochem. Soc. 148 (2001) A1324–A1335.
[31] D. Natarajan, T. Van Nguyen, J. Power Sources 115 (2003) 66–80.
[32] C.Y. Wang, Chem. Rev. 104 (2004) 4727–4765.
[33] R.B. Bird, W.E. Stewart, E.N. Lightfoot, Transport Phenomena, second ed., Wiley, New York, 2002.
[34] J.C. Amphlett, R.M. Baumert, R.F. Mann, B.A. Peppley, P.R. Roberge, T.J. Harris, J. Electrochem. Soc. 142 (1995) 1–8.